

Wave-Former: Through-Occlusion 3D Reconstruction via Wireless Shape Completion

Laura Dodds¹, Maisy Lam¹, Waleed Akbar¹, Yibo Cheng¹, Fadel Adib^{1,2}

¹ - Massachusetts Institute of Technology, ² - Cartesian Systems

{ldodds, mllam, wakbar, yiboc, fadel}@mit.edu

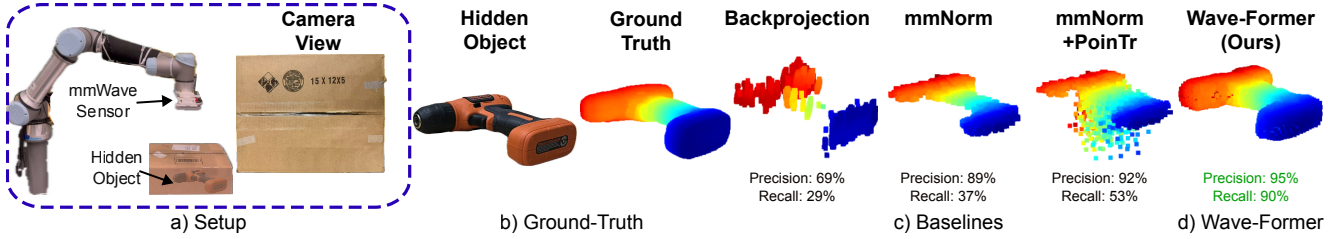


Figure 1. **Wave-Former:** a) Wave-Former can reconstruct objects hidden inside closed boxes using a millimeter-wave sensor. b) The ground-truth RGB and point cloud of a hidden object. c) Two state-of-the-art mmWave reconstruction methods (Backprojection and mmNorm) cannot reconstruct the entire object shape. Simply applying vision-based shape completion models (PoinTr) produces noisy reconstructions. d) By incorporating mmWave physical properties, Wave-Former can reconstruct the complete 3D shape of a hidden object from mmWave signals.

Abstract

We present Wave-Former, a novel method capable of high-accuracy 3D shape reconstruction for completely occluded, diverse, everyday objects. This capability can open new applications spanning robotics, augmented reality, and logistics. Our approach leverages millimeter-wave (mmWave) wireless signals, which can penetrate common occlusions and reflect off hidden objects. In contrast to past mmWave reconstruction methods, which suffer from limited coverage and high noise, Wave-Former introduces a physics-aware shape completion model capable of inferring full 3D geometry. At the heart of Wave-Former’s design is a novel three-stage pipeline which bridges raw wireless signals with recent advancements in vision-based shape completion by incorporating physical properties of mmWave signals. The pipeline proposes candidate geometric surfaces, employs a transformer-based shape completion model designed specifically for mmWave signals, and finally performs entropy-guided surface selection. This enables Wave-Former to be trained using entirely synthetic point-clouds, while demonstrating impressive generalization to real-world data. In head-to-head comparisons with state-of-the-art baselines, Wave-Former raises recall from 54% to 72% while maintaining a high precision of 85%.

1. Introduction

Reconstructing the 3D geometry of a fully occluded object, such as one inside a closed box or beneath clutter, is an open challenge in computer vision. This capability could enable numerous applications spanning robotic manipulation, augmented reality, and shipping and logistics. However, optical

sensors, such as cameras and LiDARs, are inherently limited in such scenarios. In contrast, radio-frequency signals, such as millimeter-waves (mmWave), can traverse through occlusions and reflect off hidden objects. This ability has inspired recent interest in using these reflections for partial reconstruction of hidden objects [14, 16].

However, estimating the complete 3D shape of hidden objects with mmWave signals remains challenging. This limitation arises from the unique physical properties of mmWave reflections. Unlike visible light, which scatters diffusely off most surfaces, mmWave signals reflect primarily in a specular (mirror-like) manner [41] (Fig. 2). As a result, large portions of the surface will reflect signals away from the mmWave sensor, causing them to be effectively invisible and severely limiting the coverage. This issue is further compounded by the fact that mmWave signals are significantly noisier¹ and capture surface reflections at much lower resolutions, making complete 3D reconstruction even more difficult. For example, we show two state-of-the-art mmWave reconstruction methods in Fig. 1 c, Backprojection [14] and mmNorm [16], on a real-world, through-occlusion experiment. Both methods only capture a small portion of the object.

To overcome this, one natural approach is to apply existing vision-based shape completion models [65, 72, 76] to these partial mmWave reconstructions. Unfortunately, this strategy fails to produce reliable reconstructions, since these existing models are designed for visible-light sensors with high coverage and resolution, and do not account

¹Compared to the Kinect depth camera, point clouds produced with mmWave signals have roughly 5× more noise [16, 35].

for the unique physical properties of mmWave reflections. For instance, we show an example in Fig. 1c where applying a state-of-the-art vision-based model, PoinTr [72], to a mmWave partial point cloud produces a highly inaccurate and noisy reconstruction.

In this paper, we present Wave-Former, the first complete mmWave 3D reconstruction method that can estimate the geometry of diverse objects through occlusions. Wave-Former bridges the gap between wireless sensing and modern shape completion techniques by embedding unique mmWave physics into the learning process. In Fig. 1d, we demonstrate that Wave-Former improves reconstruction quality on a real-world through-occlusion example, where the object is completely hidden from view.

Our core idea is a physics-aware training framework that embeds the physical characteristics of mmWave signals directly into the learning process. We train a transformer-based shape completion network entirely on synthetic 3D point clouds (e.g., ShapeNet [10]) while introducing a specularity-aware inductive bias that models the sparse, specular reflections of mmWave signals. Furthermore, our framework incorporates reflection-dependent visibility patterns, enabling the model to anticipate regions of the object that may be inherently unobserved. Finally, to enhance robustness against real-world noisy measurements, we adapt the model’s loss function to jointly refine the noisy input and complete missing surfaces.

We then incorporate this design into a real-world inference process that transforms raw mmWave signals into several candidate surface hypotheses, applies our physics-aware shape completion model to each, and performs entropy-guided surface selection to output a single high-fidelity 3D reconstruction.

Our approach achieves state-of-the-art results on through-occlusion reconstruction. Across 61 diverse objects from the YCB dataset [9], Wave-Former achieves a 72% recall, an 18% improvement over the next-best baseline, while maintaining a high precision of 85%.

Contributions. We summarize our main contributions:

- **Physics-Aware mmWave Shape Completion.** We introduce the first through-occlusion mmWave 3D shape completion framework for diverse objects. It features a physics-aware training pipeline and real-world inference process, which together enable training entirely on synthetic data while showing 3D reconstruction on real-world data.
- **State-of-the-Art Performance.** On the real-world MITO dataset [15], we boost recall from 54% to 72% over existing mmWave reconstruction methods, (Backprojection [14], mmNorm [16], RMap [46]), while retaining 85% precision.
- **Ablation Study Against Vanilla Vision-Based Models.** We outperform vanilla vision-based completion models applied to mmWave partials, increasing recall by 12% and achieving the highest precision of 85%.

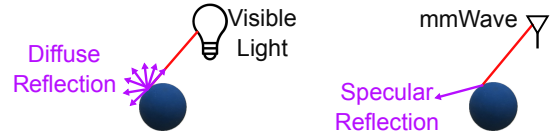


Figure 2. **Specular reflection.** Unlike visible light, which primarily scatters, mmWave signals undergo primarily specular (mirror-like) reflections.

2. Related Work

Shape Completion in Visible Spectrum. Shape completion in the visible spectrum has been a long-standing problem in computer vision, with methods evolving from early geometric approaches [4–6, 32] and encoder-decoder architectures [56, 73] to more recent transformer- and diffusion-based frameworks [7, 17, 31, 39, 43, 62, 65, 69, 72, 76, 77]. These models achieve remarkable performance on synthetic, camera, and LiDAR datasets, benefiting from point clouds with relatively high coverage and low noise compared to mmWave partial observations. However, these models are not directly applicable to the mmWave domain, as they fail to capture the physical characteristics of mmWave propagation, such as specularity, low spatial resolution, and low signal-to-noise ratios (SNRs). Consequently, vision-based completion methods struggle to recover reliable geometry from mmWave point clouds (as we demonstrate empirically in Sec. 5.3), underscoring the need for architectures that explicitly account for mmWave-specific physical properties.

mmWave Imaging. The vast majority of work in the mmWave space can image and reconstruct only the radar-facing surfaces of occluded objects or scenes, since they operate based on reflections that return from the surface. This includes volumetric [8, 14, 37, 38], interferometric [18–20, 22], surface-normal based [16] estimation approaches, as well as learning-based image enhancement [1, 23, 29, 30, 50] and scene reconstruction [21, 42, 46, 48, 61, 74]. This limitation is why airport mmWave scanners [45, 47] require a large infrastructure to rotate antennas around the entire human body, and require a large non-commercially available bandwidth to achieve high-accuracy depth estimation. In contrast, Wave-Former is able to perform complete 3D reconstruction with limited coverage of an object and only commercially available bandwidth through a physics-aware shape completion pipeline.

Additionally, some prior works have investigated mmWave full mesh reconstruction by focusing on a very limited set of objects (i.e., one to five categories) through strong data priors. For example, some works can only reconstruct humans due to their strong assumptions about human morphology [11, 66–68, 70, 71, 75]. Similarly, other work can only reconstruct up to five categories of objects (chairs, cars, robot arms, boxes, and desks) [52–54]. These works are fundamentally limited due to the fact that real-world and simulated mmWave data is extremely scarce. In contrast, Wave-Former eliminates the need for real-world

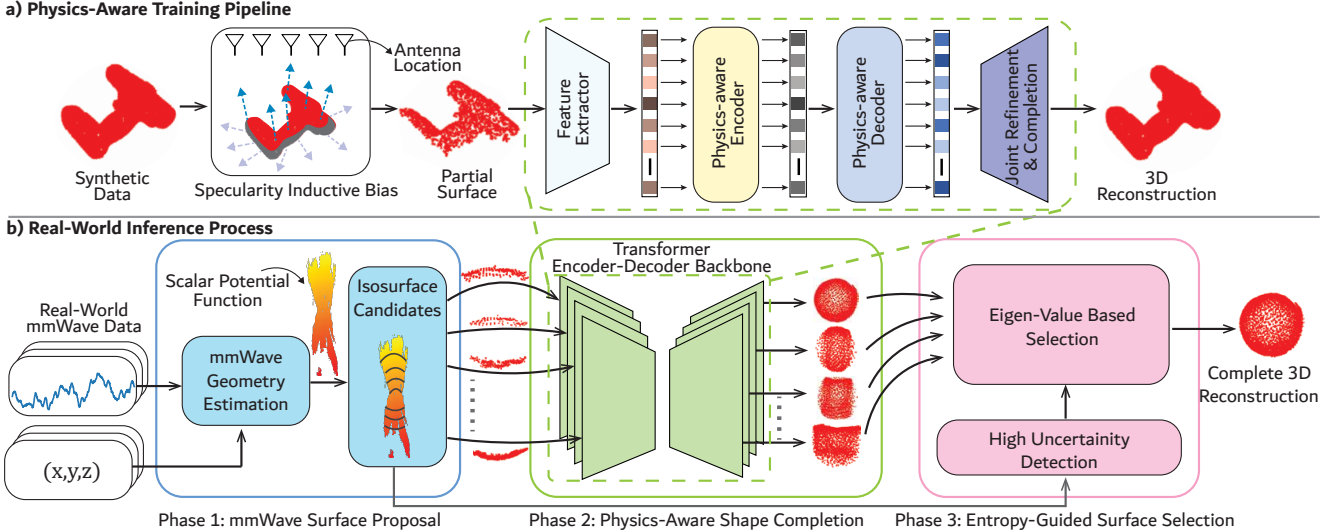


Figure 3. **mmWave Reconstruction Pipeline.** a) Wave-Former’s physics-aware training pipeline incorporates physical properties through a specularity-aware inductive bias, reflection-dependent visibility, and joint refinement and completion framework to enable training on entirely synthetic data. b) Wave-Former’s real-world inference process leverages a three-stage pipeline to reconstruct a complete 3D object from real mmWave signals.

mmWave training data by incorporating physical mmWave properties with readily-available synthetic 3D datasets, thus enabling generalization to diverse objects.

Alternative Through-Occlusion Perception Modalities. Recovering geometry through occlusions has been explored with various sensing modalities. For example, X-rays can penetrate opaque materials but use ionizing radiation, making them unsuitable for extended human exposure [59]. Additionally, acoustic or ultrasound is impractical for imaging through closed boxes due to the change in material properties (i.e., impedance mismatch) between air and cardboard [33].² Furthermore, thermal imaging [26, 28, 44, 49] can only image objects via heat, and thus is more suitable for imaging living things (due to their body temperature) rather than inanimate objects. Finally, around-the-corner laser [12, 24, 27, 34, 58] imaging can produce images in non-line-of-sight settings but cannot perceive through opaque obstacles, making them ill-suited for scenarios where objects are in a closed box or beneath clutter. In contrast, mmWave sensing combines material penetration and human safety, making it a practical modality for through-occlusion perception [14, 16, 23, 25, 25, 36, 40, 60, 68].

3. Preliminaries

Here, we describe the process of classical mmWave imaging at a high-level, and refer readers to [57] for more details.

Forming Images from mmWave Signals. Millimeter-wave (mmWave) radars transmit a frequency-modulated continuous wave (FMCW) signal which travels through occluding materials and reflects off hidden objects before being received back at the radar. These reflections carry information about how far the wave traveled, as a frequency

shift, and the direction from which they arrived, as phase shifts across sensor locations. Together, this allows us to reconstruct a 3D image of the radar-facing surface of the object, where the image value $S(v)$ at each voxel v estimates the power reflected from that point in space [2]:

$$S(v) = \sum_{k=1}^N \sum_{t=1}^T h_k(t) e^{j2\pi(2||p_k - v||)/\lambda_t} \quad (1)$$

where p_k is the k^{th} sensor location, λ_t is the wavelength of the t^{th} sample (out of T), and $h_k(t)$ is the t^{th} sample of the time-domain baseband received signal from the k^{th} location.

Specularity. One primary limitation of these 3D mmWave images is that they only measure the radar-facing surface of an occluded object. Specifically, since mmWave signals experience primarily specular (mirror-like) reflections [41], many parts of an object’s surface will reflect signals away from the sensor and thus are not present in the image. Wave-Former overcomes this limitation by bridging raw mmWave signals with physics-aware shape-completion.

4. Method

We design Wave-Former to perform high-fidelity, complete 3D reconstruction of hidden objects leveraging mmWave signals. Our core insight lies in a physics-aware training pipeline (Fig. 3a) to enable learning shape completion for mmWave properties using entirely synthetic data (Sec. 4.2). We additionally propose a real-world inference process (Fig. 3b) that (1) converts raw, mmWave signals into candidate partial surface representations (Sec. 4.3.1), (2) performs physics-aware shape completion (Sec. 4.3.2), and (3) identifies the optimal reconstruction (Sec. 4.3.3).

4.1. Problem Definition

Our goal is to reconstruct a complete 3D point cloud \hat{F} of a fully occluded object from a sequence of raw, complex-

²Gel minimizes the mismatch when imaging through human tissue [3].

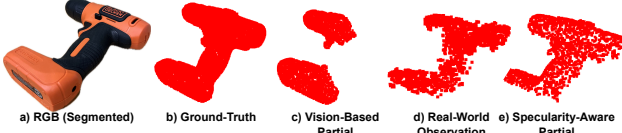


Figure 4. **Specularity-Aware Inductive Bias.** Specularity-aware inductive bias generates training partials (e) that resemble real mmWave visibility (d), unlike standard masking used in vision-based models (c).

valued, time-domain mmWave measurements. Let $H \in \mathbb{C}^{N \times T}$ denote the collection of all measurements acquired from N known sensor positions $P \in \mathbb{R}^{N \times 3}$, where each sensor position yields T temporal samples. Our pipeline learns a mapping $f_\theta : (H, P) \mapsto \hat{F}$.

4.2. Physics-Aware Training Pipeline

Training a shape-completion model for mmWave signals is fundamentally different from training one for visible-light sensors, such as cameras or LiDAR. Millimeter-wave returns are specular, anisotropic, and noisy, while existing completion models are trained on vision-like partials, which implicitly assume diffuse reflections and wide, uniform coverage, making them ill-suited for mmWave inputs.

To overcome this, our key insight is to embed mmWave physics directly into the training data and objective, creating a physics-consistent observation model that teaches the network physically plausible mmWave shape completion. By doing so, we enable training entirely on readily-available synthetic 3D datasets while achieving state-of-the-art generalization to real mmWave signals, as shown in Sec. 5.2.

4.2.1. Specularity-Aware Inductive Bias

Existing vision-based completion models inherently encode inductive bias consistent with visible light and incompatible with mmWave signals. This arises from their camera-like partial observations which assume diffuse reflections and wide coverage. To address this, we reformulate the inductive bias with physically consistent partials which emulate the specular reflections of mmWave signals. Specifically, for a given 3D model, we only include points in our partial which 1) produce a specular return and 2) lie on the radar facing surface (and are not further occluded by the object itself). Formally, we create partial observations O as:

$$O = \left\{ s_i \in F \mid \theta_P(s_i) < \tau \cap V(s_i) = 1 \right\} \quad (2)$$

where s_i is a point in the full 3D cloud F . $\theta_P(s_i)$ denotes the smallest angular mismatch between s_i and all sensor positions in P . It is defined as $\theta_P(s_i) = \min_{k \in P} |\text{acos}(n_i \cdot u_{k,i})|$ where n_i is the normal at point s_i and $u_{k,i} = (p_k - s_i) / \|p_k - s_i\|$ is the unit vector pointing from s_i to p_k . $V(s_i)$ is 1 when a point s_i lies on a radar facing surface and 0 otherwise.³

Applying this inductive bias during training teaches the model to expect mmWave-specific partial observations,

³We compute this using Open3D’s `hidden_point_removal`.

guiding it to focus on physically plausible surfaces. This results in more accurate reconstructions and better generalization to real-world mmWave measurements (See Sec. 5.4).

4.2.2. Reflection-Dependent Visibility

Unlike optical sensors, mmWave visibility is strongly anisotropic: the measurable reflections depend on the incident angles and the reflection strength of an object. As a result, two objects with the same geometry may have markedly different visibility depending on their material properties. To model this behavior, we introduce a reflection-dependent visibility pattern that attenuates surface points according to physically-guided angular and material constraints. This replaces the common assumption of isotropic coverage and teaches the network that mmWave visibility is inherently non-uniform and angle dependent. Formally, for each specularity-aware partial O , we generate anisotropic partials O_A as:

$$O_A = \{s_i \in O \mid \theta_H(n_i) < \tau_H \cap \theta_V(n_i) < \tau_V\} \quad (3)$$

where $\theta_H = |\text{acos}(n_i \cdot [1, 0, 0])|$ and $\theta_V = |\text{acos}(n_i \cdot [0, 1, 0])|$ are the angles of the specular return from point s_i in the horizontal and vertical dimensions. τ_H and τ_V are parameters that can be changed to simulate different material properties. We train across a range of parameters to ensure robust mmWave completion.

Combined with our specularity-aware inductive bias, this visibility pattern further constrains the model to learn from physically plausible partial observations.

4.2.3. Joint Refinement and Completion

Existing vision-based shape completion models are designed for noise and resolution properties typical of a camera or LiDAR sensor, and therefore assume input partials can be directly concatenated with the reconstructed points. However, mmWave signals experience significantly higher noise levels (e.g., up to 5× higher than depth-camera point clouds [16, 35]) and a reduction in resolution. Thus, existing concatenation strategies would propagate significant distortions into the final reconstruction.

To address this, we introduce a joint refinement and completion method. Instead of preserving a noisy partial, we allow the model to simultaneously denoise and complete the object. To enable this, we incorporate noise during training to reflect the behavior of real-world mmWave signals. Then, we reformulate the loss function to allow the model to output the complete 3D shape (without concatenating the input), allowing it to reinterpret unreliable points rather than preserve them. Formally, we define the loss as the bi-directional chamfer distance between the complete, denoised output, \hat{F} and the ground-truth shape, F :

$$\mathcal{L} = \frac{1}{|\hat{F}|} \sum_{s_i \in \hat{F}} \min_{g \in F} \|s_i - g\| + \frac{1}{|F|} \sum_{g \in F} \min_{s_i \in \hat{F}} \|g - s_i\| \quad (4)$$

This method further improves Wave-Former’s generalization to real-world measurements, as we show empirically in Sec. 5.4

Together, these three techniques establish a new physics-aware learning paradigm for mmWave shape completion, enabling state-of-the-art through-occlusion reconstruction capabilities.

Physics-Aware Encoder-Decoder We integrate the above techniques into a transformer-based encoder-decoder for shape completion which maps a partial observation to an estimate of the complete 3D geometry: $\hat{F} = f_p(O)$. Built on the PoinTr backbone [72], our encoder-decoder is trained with a physics-consistent observation model (Eqs. 2 and 3) and a denoising-completion objective (Eq. 4), biasing the learned representation toward physically plausible mmWave surfaces. Our techniques enable us to train entirely with large, readily available synthetic 3D datasets [13, 51, 64], without relying on scarcely available real-world mmWave data. Critically, this allows Wave-Former to generalize to many different objects.

4.3. Real-World Inference Process

After training a physics-aware shape completion model, we next develop an inference process that converts raw, real-world mmWave signals into complete 3D reconstructions (Fig. 3b). Our pipeline follows three phases: mmWave surface proposal, physics aware shape completion, and entropy-guided surface selection.

4.3.1. Phase 1: mmWave Surface Proposal

We first transform raw mmWave measurements into a set of candidate partial surfaces which accurately capture the geometric information contained in the reflections.

Typically, partial mmWave point cloud estimation relies on thresholding a mmWave 3D power image (Eq. 1). However, this results in point clouds with significant erroneous points, as shown by the Backprojection baseline in Sec. 5.2. Instead, we leverage recent advancements in mmWave imaging [16] which can transform raw reflections into a space of geometrically consistent partial surfaces.

Formally, we compute a scalar potential function $f(v)$ consistent with mmWave reflections, where each isosurface⁴ of this function is one possible partial surface [16]:

$$f(v) = \sum_{j \in R} N(v_j) \cdot d_j \quad (5)$$

where $N(v_j)$ is the estimated mmWave normal vector field, and $f(v_0) = 0$ at a reference voxel v_0 , and R is the discrete path connecting v_0 and v . The value $f(v)$ represents the accumulated field integral along R , and d_j is the direction vector along R pointing from v_{j-1} to v_j .

Unlike prior approaches which directly attempt to estimate the best candidate surface, we instead summarize the

⁴An isosurface is a surface of a constant value within a function.

entire physically-plausible partial space by sampling candidate surfaces throughout this scalar function. This preserves available geometric information used during shape completion, and prevents critical errors caused by prematurely selecting the wrong surface. Formally:

$$C_{p,i} = \{v \mid |f(v) - I(i)| < \delta\} \quad (6)$$

where $C_{p,i}$ is the i^{th} candidate partial surface, $I(i)$ is the value of the i^{th} isosurface we sample, and δ is a small constant to account for numerical discrepancies.

4.3.2. Phase 2: Physics-Aware Shape Completion

Next, we convert the space of partial observations into a space of complete 3D reconstructions. We apply our physics-aware shape completion model, trained to incorporate physical properties as described in Sec. 4.2, to each candidate partial surface. This produces a set of physically-plausible candidate complete reconstructions, $C_{F,i}$:

$$C_{F,i} = f_p(C_{p,i}) \quad (7)$$

4.3.3. Phase 3: Entropy-Guided Surface Selection

In our final phase, we identify the optimal reconstruction from the space of candidate reconstructions.

Under high signal-to-noise conditions, we follow prior work [16] and select the optimal surface by comparing the simulated mmWave response of each candidate to the measured signals. However, when reflections are weak and the normal field contains significant noise, this often leads to erroneous surface selection. To handle these challenging cases, we introduce an entropy-guided selection strategy.

Detecting High-Uncertainty Reconstructions. We identify partial observations corrupted by noise, where weak reflections or noisy normals cause the scalar field $f(v)$ (Eq. 5) to produce irregular, vertically stacked voxels instead of smooth isosurfaces. We use the vertical spread of these voxels to serve as a proxy for reconstruction uncertainty. Formally, we classify reconstructions as high uncertainty when $\frac{|C_{p,i}^{xy}|}{|C_{p,i}|} > 0.6$, where $C_{p,i}^{xy}$ is constructed by projecting the observation $C_{p,i}$ to 2D and removing duplicate points.

Determining the Optimal Reconstruction. For high-uncertainty cases, we observe that physically consistent inputs produce continuous, locally planar reconstructions, whereas inaccurate or noisy inputs yield high-entropy point clouds dispersed over a larger spatial volume. We therefore select the candidate reconstruction with the lowest degree of local entropy.

We quantify entropy by sampling local neighborhoods⁵ and computing the covariance eigenvalues $\lambda_1 \geq \lambda_2 \geq \lambda_3$. Since planar regions have two dominant eigenvalues, whereas high-entropy regions have three of similar magnitude, we define an entropy score λ_3/λ_1 [63]. We then combine this score across all neighborhoods, and select the

⁵We use kNN with k=30.

reconstruction with the smallest ratio:

$$i^* = \arg \min_i \left(\text{pcnt1} \left(\left\{ \frac{\lambda_{3,p}}{\lambda_{1,p}} \forall p \in C_{F,i} \right\}, 75 \right) \right) \quad (8)$$

Then, our final surface selection is $\hat{F} = C_{F,i^*}$.

Together, these three phases together output a single, high-fidelity 3D reconstruction of a fully occluded object.

5. Experiments

5.1. Dataset and Implementation

Datasets: To train Wave-Former, we leverage three publicly available 3D object datasets: OmniObject3D [64], Toys4K-3D [51], and the Thingiverse subset of Objaverse [13], totaling over 25K 3D object point clouds.

We evaluate Wave-Former on a real-world dataset of mmWave measurements, MITO [15]. The dataset contains measurements of 61 objects from the YCB dataset [9]. These items consist of a diversity of tasks (kitchen items, tools, food items, toys, etc), materials (wood, metal, cardboard, plastic, etc), and geometries (complex shapes, sharp edges, flat and curved surfaces, etc). This includes experiments in both line-of-sight and fully occluded settings for each object. More details can be found in [15].

Training: We train our model using exclusively synthetic data, using the techniques in Sec 4.2. Each of the synthetic datasets are shuffled and split into 80% for training and 20% for testing. Additional details can be found in A.1.

Evaluation: For real-world evaluation, we directly input the raw mmWave radar data into Wave-Former without any additional masking or augmentations. We compare to the ground-truth 3D reconstructions provided in the MITO dataset [15]. Following prior work [65, 72], we align the reconstructed partial point clouds generated in Sec. 4.3.1 with the ground-truth point cloud for inference and evaluation.

Evaluation Metrics: We adopt four standard metrics [55]: Chamfer Distance (CD), Precision, Recall, and F-Score, which jointly assess the accuracy and completeness of the reconstructions. We provide detailed definitions in A.2.

Baselines: We evaluate our approach against four state-of-the-art mmWave reconstruction baselines. We include detailed descriptions in A.3:

- *Backprojection* [14]: This is the classical and most widely used mmWave imaging approach. It is a first-principle method for volumetric mmWave reconstruction.
- *mmNorm* [16]: This is a recently-introduced state-of-the-art mmWave 3D reconstruction approach. It is also a first-principle method which estimates surface normal vectors and uses them to reconstruct the surface of the object
- *RMap* [46]: This is a state-of-the-art learning-based method for mmWave reconstruction, originally designed for scene level understanding. This model expects mmWave point cloud inputs, so we use mmNorm to create the input.
- *RMap (Finetuned)* [46]: We finetune RMap for object reconstruction on the same training data as Wave-Former.

5.2. Baseline Comparisons

5.2.1. Qualitative Results

To start, we compare qualitative results across Wave-Former and all four baselines using real-world measurements. Fig. 5 shows an isometric view of the ground-truth RGB (segmented) and point cloud, as well as the reconstruction for each method across several fully-occluded objects. Wave-Former is able to consistently reconstruct the complete shape of the object, even for complex geometries such as a power drill and clamp. In contrast, the baselines suffer from low accuracy, limited coverage, high noise, and, in some cases, even a complete lack of discernible geometry. These results demonstrate the significant advancement of Wave-Former over prior state-of-the-art mmWave 3D reconstruction methods.

5.2.2. Quantitative Results

Table 1 reports the average chamfer distance, F-Score, precision, and recall across Wave-Former and all baselines. Notably, Wave-Former achieves a significant increase in recall, from 54% to 72% over the best-performing baseline, RMap (Finetuned), while maintaining a high precision of 85%.⁶ Additionally, Wave-Former achieves the lowest chamfer distance of 0.069, compared to 0.18 for the best-performing baseline. This demonstrates the value of our techniques for enabling complete and high-accuracy 3D reconstruction of fully occluded objects.

5.3. Comparison to Vision-Based Shape Completion

We also evaluate whether state-of-the-art vanilla vision-based shape completion models can achieve high-accuracy mmWave 3D reconstruction. To produce radar-visible partial point clouds, we use the state-of-the-art mmWave reconstruction baseline with the highest precision per Table 1 (mmNorm), which is then fed into vision-based completion models. To ensure a fair comparison, all models are fine-tuned with the same synthetic datasets as used to train Wave-Former, while applying their own partial point cloud creation strategies. Table 2 reports the performance of Wave-Former compared to four state-of-the-art models. Wave-Former outperforms all models across all metrics, achieving an increase in recall from 60% to 72%, while also achieving the highest precision of 85%. This shows the importance of incorporating physical properties into the shape completion model. We also provide qualitative examples of Wave-Former compared to each vanilla shape completion model in A.4.

5.4. Ablation Study

Next, we analyze how different components of Wave-Former’s design contribute to the overall performance. Table 3 shows the average and 75th percentile CD, as well as the marginal percent increase, of Wave-Former

⁶mmNorm shows slightly higher precision since, as a first-principles method, it does not infer full geometry, leading to much lower recall.

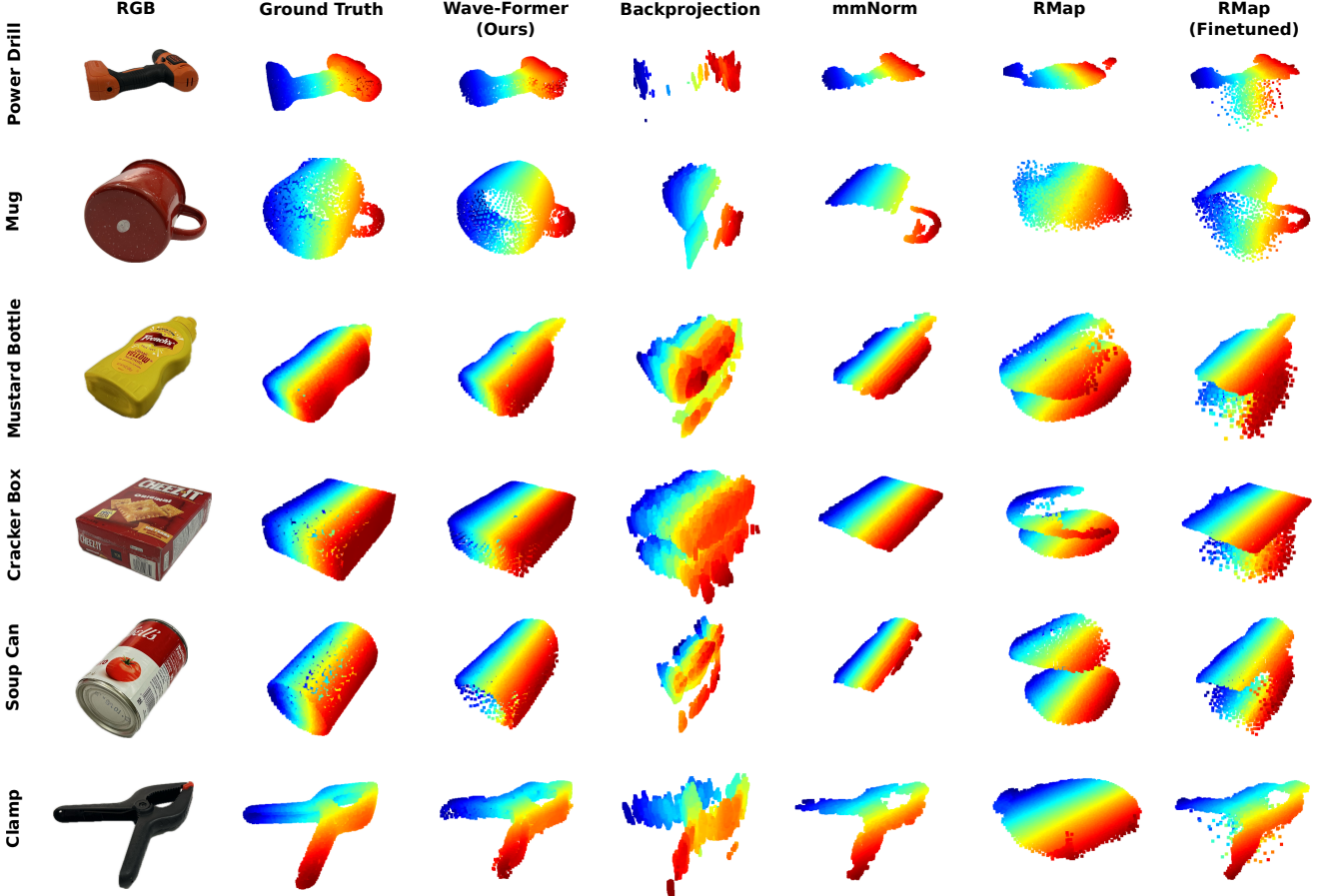


Figure 5. **Qualitative Results.** Visual comparison of mmWave 3D reconstruction on real-world, fully occluded objects. State-of-the-art baselines suffer from artifacts such as high noise and limited coverage, while Wave-Former consistently reconstructs shapes with high fidelity.

	CD ↓	FS ↑	Precision ↑	Recall ↑
Backprojection [14]	0.180	40%	43%	45%
mmNorm [16]	0.214	45%	89%	34%
R-Map [46]	0.273	23%	40%	17%
R-Map (Finetuned) [46]	0.330	62%	81%	54%
Wave-Former	0.069	75%	85%	72%

Table 1. Comparison between Wave-Former and state-of-the-art mmWave reconstruction baselines.

compared to three different partial implementations. First, when removing our specularity-aware inductive bias and reflection-dependent visibility (model A), we see a significant drop in performance, with the average chamfer distance increasing by 52% and the 75th percentile increasing by 67%. Next, when also removing our joint reconstruction and completion (model B), average chamfer distance increases by an additional 10%. Finally, when also removing our entropy-aware surface selection (model C), the 75th percentile continues to increase an additional 19%. We further demonstrate the benefit of our entropy-aware surface selection through qualitative examples in A.5, which show that for some objects, our selection process leads to drastically improved reconstructions.

	CD ↓	FS ↑	Precision ↑	Recall ↑
mmNorm + PoinTr	0.104	62%	81%	53%
mmNorm + SnowFlakeNet	0.097	66%	80%	60%
mmNorm + SeedFormer	0.095	66%	83%	59%
mmNorm + PCN	0.138	58%	70%	56%
Wave-Former	0.069	75%	85%	72%

Table 2. Comparison with state-of-the-art vision-based vanilla shape completion models applied to the state-of-the-art mmWave reconstruction method.

Together, these results demonstrate how each component of Wave-Former contributes to its overall performance.

Model	Average			75 th Pctl	
	Physics	JRAC	Entropy	CD	% Inc.
Wave-Former	✓	✓	✓	0.069	—
A		✓	✓	0.105	52%
B			✓	0.115	10%
C				0.116	1%

Table 3. Ablation study of average and 75th percentile CD, as well as marginal % increase, for different components of Wave-Former.

5.5. Microbenchmarks

We performed microbenchmark experiments to understand the impact of various factors on Wave-Former.

5.5.1. Impact of Occlusions

	Line-of-Sight		Fully Occluded	
	CD ↓	F-Score ↑	CD ↓	F-Score ↑
Backprojection [14]	0.177	40%	0.183	40%
mmNorm [16]	0.198	46%	0.231	44%
R-Map [46]	0.273	23%	0.272	24%
R-Map (Finetuned) [46]	0.091	64%	0.581	61%
Wave-Former	0.058	78%	0.080	73%

Table 4. Average performance in line-of-sight & fully occluded settings.

First, we compare the performance of Wave-Former and all baselines in line-of-sight and fully-occluded settings. Table 4 reports the average chamfer distance and F-Score. Notably, Wave-Former performs similarly in both settings, experiencing only a minor decrease in performance in fully-occluded settings. This demonstrates the ability of Wave-Former to not only reconstruct objects in visual line of sight, but also objects that are fully hidden from view.

5.5.2. Impact of Object Size

	Large	Medium	Small
Backprojection [14]	0.092	0.152	0.293
mmNorm [16]	0.078	0.201	0.361
R-Map [46]	0.136	0.239	0.452
R-Map (Finetuned) [46]	0.057	0.621	0.158
Wave-Former	0.044	0.057	0.109
Improvement	0.013	0.095	0.049

Table 5. Average CD for different object sizes.

Next, we evaluate the performance of Wave-Former and all baselines across objects of different sizes. We divide all objects into three categories based on their longest dimension: Large (>20 cm), Medium (10 cm-20 cm), and Small (<10 cm). Table 5 reports the average chamfer distance across different object sizes. As expected, Wave-Former performs best for large objects, with a chamfer distance of 0.04, compared to 0.06 for the best-performing baseline. As objects decrease in size, mmWave perception becomes increasingly challenging (See A.6).

5.5.3. Impact of mmWave Coverage

	Moderate	Challenging	Extreme
Backprojection [14]	0.076	0.140	0.325
mmNorm [16]	0.064	0.155	0.434
R-Map [46]	0.126	0.221	0.481
R-Map (Finetuned) [46]	0.050	0.076	0.904
Wave-Former	0.033	0.048	0.126
Improvement	0.017	0.028	0.199

Table 6. Average CD for different initial object coverage.

Finally, we assess how varying levels of coverage affect the performance of Wave-Former. To start, we compute the percent of ground-truth points “covered” by the mmWave

partial observation, where a point is considered covered if its nearest neighbor in the input lies within 0.08 m (for objects scaled to a unit sphere). We then define three categories of objects: Moderate ($>36\%$), Challenging (18%-36%), and Extreme ($<18\%$).⁷ It is important to note that these percentages are significantly more challenging than most standard vision-based shape completion models, which only consider point clouds with 25% to 75% coverage [72, 76]. This is due to the specular reflections of mmWave signals, which result in significantly lower coverage than visible light.

Table 6 reports the average chamfer distance of Wave-Former and all baselines. In all categories, Wave-Former outperforms all baselines. As the objects become more challenging, Wave-Former outperforms the best baseline by an increasing amount, with a 0.2 improvement for the Extreme category. This highlights the benefit of our techniques for enabling through-occlusion 3D mmWave reconstruction even on extremely challenging examples. We also show qualitative examples from each category in A.7.

6. Conclusion & Future Opportunities

We presented Wave-Former, the first mmWave 3D reconstruction method that can operate on fully-occluded, diverse, everyday objects. Wave-Former leverages a novel physics-aware training pipeline to integrate core physical properties of mmWave signals into the completion process. Then, Wave-Former uses a real-world inference process which proposes candidate surfaces, leverages our physics-aware shape completion model, and selects a final reconstruction. These techniques allow Wave-Former to be trained on entirely synthetic 3D data while demonstrating impressive generalization to real-world signals.

Building on these contributions, we believe Wave-Former opens up many exciting directions for future research. For example, it would be interesting to use Wave-Former to develop novel downstream capabilities, such as fully-occluded robotic grasping, augmented reality with through-occlusion perception, or automatic package verification in shipping and logistics. Additionally, as the first paper to tackle the challenge of diverse mmWave 3D reconstruction, we hope that Wave-Former inspires future research towards reconstruction with even higher fidelity or using increasingly smaller radar scans. Finally, our techniques for training entirely on synthetic data may bring benefit to other mmWave tasks, such as fully-occluded classification, segmentation, and pose estimation.

More generally, we hope this work marks an important step towards generalizable through-occlusion perception.

⁷Thresholds were selected for balanced category distribution.

References

[1] Aakriti Adhikari, Hem Regmi, Sanjib Sur, and Srihari Nelakuditi. Mishape: Accurate human silhouettes and body joints from commodity millimeter-wave devices. *Proceedings of the ACM on Interactive, Mobile, Wearable and Ubiquitous Technologies*, 6(3):1–31, 2022. 2

[2] Fadel Adib, Chen-Yu Hsu, Hongzi Mao, Dina Katabi, and Frédo Durand. Capturing the human figure through a wall. *ACM Transactions on Graphics (TOG)*, 34(6):219, 2015. 3

[3] John E Aldrich. Basic physics of ultrasound imaging. *Critical care medicine*, 35(5):S131–S137, 2007. 3

[4] Marc Alexa, Johannes Behr, Daniel Cohen-Or, Shachar Fleishman, David Levin, and Claudio T Silva. Point set surfaces. In *Proceedings Visualization, 2001. VIS’01.*, pages 21–29. IEEE, 2001. 2

[5] Nina Amenta, Marshall Bern, and Manolis Kamvysselis. A new voronoi-based surface reconstruction algorithm. In *Proceedings of the 25th annual conference on Computer graphics and interactive techniques*, pages 415–421, 1998.

[6] Nina Amenta, Sunghee Choi, and Ravi Krishna Kolluri. The power crust. In *Proceedings of the sixth ACM symposium on Solid modeling and applications*, pages 249–266, 2001. 2

[7] Burak Bekci, Nassir Navab, Federico Tombari, and Mahdi Saleh. Escape: Equivariant shape completion via anchor point encoding. In *Proceedings of the Computer Vision and Pattern Recognition Conference*, pages 6480–6489, 2025. 2

[8] Pingping Cai and Sanjib Sur. Millipcd: Beyond traditional vision indoor point cloud generation via handheld millimeter-wave devices. *Proceedings of the ACM on Interactive, Mobile, Wearable and Ubiquitous Technologies*, 6(4):1–24, 2023. 2

[9] Berk Calli, Arjun Singh, James Bruce, Aaron Walsman, Kurt Konolige, Siddhartha Srinivasa, Pieter Abbeel, and Aaron M Dollar. Yale-cmu-berkeley dataset for robotic manipulation research. *The International Journal of Robotics Research*, 36(3):261–268, 2017. 2, 6

[10] Angel X. Chang, Thomas Funkhouser, Leonidas Guibas, Pat Hanrahan, Qixing Huang, Zimo Li, Silvio Savarese, Manolis Savva, Shuran Song, Hao Su, Jianxiong Xiao, Li Yi, and Fisher Yu. ShapeNet: An Information-Rich 3D Model Repository. Technical Report arXiv:1512.03012 [cs.GR], Stanford University — Princeton University — Toyota Technological Institute at Chicago, 2015. 2

[11] Anjun Chen, Xiangyu Wang, Kun Shi, Shaohao Zhu, Bin Fang, Yingfeng Chen, Jiming Chen, Yuchi Huo, and Qi Ye. Immfusion: Robust mmwave-rgb fusion for 3d human body reconstruction in all weather conditions. *arXiv preprint arXiv:2210.01346*, 2022. 2

[12] Wenzheng Chen, Simon Daneau, Fahim Mannan, and Felix Heide. Steady-state non-line-of-sight imaging. In *Proceedings of the IEEE/CVF Conference on Computer Vision and Pattern Recognition*, pages 6790–6799, 2019. 3

[13] Matt Deitke, Ruoshi Liu, Matthew Wallingford, Huong Ngo, Oscar Michel, Aditya Kusupati, Alan Fan, Christian Laforte, Vikram Voleti, Samir Yitzhak Gadre, Eli VanderBilt, Aniruddha Kembhavi, Carl Vondrick, Georgia Gkioxari, Kiana Ehsani, Ludwig Schmidt, and Ali Farhadi. Objaverse-xl: A universe of 10m+ 3d objects. *arXiv preprint arXiv:2307.05663*, 2023. 5, 6

[14] Laura Dodds, Hailan Shanbhag, Junfeng Guan, Saurabh Gupta, and Haitham Hassanieh. Around the corner mmwave imaging in practical environments. In *Proceedings of the 30th Annual International Conference on Mobile Computing and Networking*, pages 1–15, 2024. 1, 2, 3, 6, 7, 8

[15] Laura Dodds, Tara Boroushaki, Cusuh Ham, and Fadel Adib. Mito: A millimeter-wave dataset and simulator for non-line-of-sight perception, 2025. 2, 6

[16] Laura Dodds, Tara Boroushaki, Kaichen Zhou, and Fadel Adib. *Non-Line-of-Sight 3D Object Reconstruction via mmWave Surface Normal Estimation*, page 445–458. Association for Computing Machinery, New York, NY, USA, 2025. 1, 2, 3, 4, 5, 6, 7, 8

[17] Yi Du, Zhipeng Zhao, Shaoshu Su, Sharath Golluri, Haoze Zheng, Runmao Yao, and Chen Wang. Superpc: a single diffusion model for point cloud completion, upsampling, denoising, and colorization. In *Proceedings of the Computer Vision and Pattern Recognition Conference*, pages 16953–16964, 2025. 2

[18] Jingkun Gao, Yuliang Qin, Bin Deng, Hongqiang Wang, and Xiang Li. A novel method for 3-d millimeter-wave holographic reconstruction based on frequency interferometry techniques. *IEEE Transactions on Microwave Theory and Techniques*, 66(3):1579–1596, 2017. 2

[19] Jingkun Gao, Yuliang Qin, Bin Deng, Hongqiang Wang, and Xiang Li. Novel efficient 3d short-range imaging algorithms for a scanning 1d-mimo array. *IEEE Transactions on Image Processing*, 27(7):3631–3643, 2018.

[20] Jingkun Gao, Bin Deng, Yuliang Qin, Xiang Li, and Hongqiang Wang. Point cloud and 3-d surface reconstruction using cylindrical millimeter-wave holography. *IEEE Transactions on Instrumentation and Measurement*, 68(12):4765–4778, 2019. 2

[21] Ruixu Geng, Yadong Li, Dongheng Zhang, Jincheng Wu, Yating Gao, Yang Hu, and Yan Chen. Dream-pcd: Deep reconstruction and enhancement of mmwave radar pointcloud. *IEEE Transactions on Image Processing*, 2024. 2

[22] Borja Gonzalez-Valdes, Yuri Alvarez-Lopez, Jose Angel Martinez-Lorenzo, Fernando Las Heras Andres, and Carey Rappaport. On the use of improved imaging techniques for the development of a multistatic three-dimensional millimeter-wave portal for personnel screening. *Progress In Electromagnetics Research*, 138:83–98, 2013. 2

[23] Junfeng Guan, Sohrab Madani, Suraj Jog, Saurabh Gupta, and Haitham Hassanieh. Through fog high-resolution imaging using millimeter wave radar. In *Proceedings of the IEEE/CVF Conference on Computer Vision and Pattern Recognition*, pages 11464–11473, 2020. 2, 3

[24] Otkrit Gupta, Thomas Willwacher, Andreas Velten, Ashok Veeraraghavan, and Ramesh Raskar. Reconstruction of hidden 3d shapes using diffuse reflections. *Optics express*, 20(17):19096–19108, 2012. 3

[25] Chenming He, Chengzhen Meng, Chunwang He, Xiaoran Fan, Beibei Wang, Yubo Yan, and Yanyong Zhang. See through vehicles: Fully occluded vehicle detection with mil-

limeter wave radar. In *Proceedings of the 30th Annual International Conference on Mobile Computing and Networking*, pages 740–754, 2024. 3

[26] Yingdong He, Hui Zhang, Edward Arens, Alexander Merritt, Charlie Huizenga, Ronnen Levinson, Andy Wang, Ali Ghahramani, and Ana Alvarez-Suarez. Smart detection of indoor occupant thermal state via infrared thermography, computer vision, and machine learning. *Building and Environment*, 228:109811, 2023. 3

[27] Felix Heide, Lei Xiao, Wolfgang Heidrich, and Matthias B Hullin. Diffuse mirrors: 3d reconstruction from diffuse indirect illumination using inexpensive time-of-flight sensors. In *Proceedings of the IEEE Conference on Computer Vision and Pattern Recognition*, pages 3222–3229, 2014. 3

[28] Marina Ivašić-Kos, Mate Krišto, and Miran Pobar. Human detection in thermal imaging using yolo. In *Proceedings of the 2019 5th International Conference on Computer and Technology Applications*, pages 20–24, 2019. 3

[29] Sakila S Jayaweera, Sai Deepika Regani, Yuqian Hu, Beibei Wang, and KJ Ray Liu. mmid: High-resolution mmwave imaging for human identification. In *2023 IEEE 9th World Forum on Internet of Things (WF-IoT)*, pages 1–6. IEEE, 2023. 2

[30] Sakila S Jayaweera, Sai Deepika Regani, Yuqian Hu, Beibei Wang, and KJ Ray Liu. Hrnet: High-resolution neural network for human imaging using mmwave radar. *IEEE Internet of Things Journal*, 2024. 2

[31] Yoni Kasten, Ohad Rahamim, and Gal Chechik. Point cloud completion with pretrained text-to-image diffusion models. *Advances in Neural Information Processing Systems*, 36: 12171–12191, 2023. 2

[32] Michael Kazhdan, Matthew Bolitho, and Hugues Hoppe. Poisson surface reconstruction. In *Proceedings of the fourth Eurographics symposium on Geometry processing*, 2006. 2

[33] Yang-Hann Kim. *Sound propagation: an impedance based approach*. John Wiley & Sons, 2010. 3

[34] Ahmed Kirmani, Tyler Hutchison, James Davis, and Ramesh Raskar. Looking around the corner using ultrafast transient imaging. *International journal of computer vision*, 95:13–28, 2011. 3

[35] Gregorij Kurillo, Evan Hemingway, Mu-Lin Cheng, and Louis Cheng. Evaluating the accuracy of the azure kinect and kinect v2. *Sensors (Basel)*, 22(7):2469, 2022. 1, 4

[36] Haowen Lai, Gaoxiang Luo, Yifei Liu, and Mingmin Zhao. Enabling visual recognition at radio frequency. In *Proceedings of the 30th Annual International Conference on Mobile Computing and Networking*, pages 388–403, 2024. 3

[37] Jaime Laviada, Ana Arboleya-Arboleya, Yuri Álvarez, Borja González-Valdés, and Fernando Las-Heras. Multiview three-dimensional reconstruction by millimetre-wave portable camera. *Scientific reports*, 7(1):6479, 2017. 2

[38] Jaime Laviada, Miguel Lopez-Portugues, Ana Arboleya-Arboleya, and Fernando Las-Heras. Multiview mm-wave imaging with augmented depth camera information. *IEEE Access*, 6:16869–16877, 2018. 2

[39] Shanshan Li, Pan Gao, Xiaoyang Tan, and Mingqiang Wei. Proxyformer: Proxy alignment assisted point cloud completion with missing part sensitive transformer. In *Proceedings of the IEEE/CVF conference on computer vision and pattern recognition*, pages 9466–9475, 2023. 2

[40] Chris Xiaoxuan Lu, Stefano Rosa, Peijun Zhao, Bing Wang, Changhao Chen, John A Stankovic, Niki Trigoni, and Andrew Markham. See through smoke: robust indoor mapping with low-cost mmwave radar. In *Proceedings of the 18th International Conference on Mobile Systems, Applications, and Services*, pages 14–27, 2020. 3

[41] Jonathan S Lu, Patrick Cabrol, Daniel Steinbach, and Ravikumar V Pragada. Measurement and characterization of various outdoor 60 ghz diffracted and scattered paths. In *MILCOM 2013-2013 IEEE Military Communications Conference*, pages 1238–1243. IEEE, 2013. 1, 3

[42] Kai Luan, Chenghao Shi, Neng Wang, Yuwei Cheng, Huimin Lu, and Xieyuanli Chen. Diffusion-based point cloud super-resolution for mmwave radar data. In *2024 IEEE International Conference on Robotics and Automation (ICRA)*, pages 11171–11177. IEEE, 2024. 2

[43] Zhaoyang Lyu, Zhifeng Kong, Xudong Xu, Liang Pan, and Dahua Lin. A conditional point diffusion-refinement paradigm for 3d point cloud completion. *arXiv preprint arXiv:2112.03530*, 2021. 2

[44] Tomohiro Maeda, Yiqin Wang, Ramesh Raskar, and Achuta Kadambi. Thermal non-line-of-sight imaging. In *2019 IEEE International Conference on Computational Photography (ICCP)*, pages 1–11. IEEE, 2019. 3

[45] Douglas McMakin, David Sheen, Thomas Hall, Jonathan Tedeschi, and A Mark Jones. New improvements to millimeter-wave body scanners. *Proceedings of 3DBODY TECH*, 2017. 2

[46] Ajay Narasimha Mopidevi, Kyle Harlow, and Christoffer Heckman. Rmap: Millimeter-wave radar mapping through volumetric upsampling. *arXiv preprint arXiv:2310.13188*, 2023. 2, 6, 7, 8

[47] National Academies of Sciences, Medicine, Division on Engineering, Physical Sciences, National Materials, Manufacturing Board, Committee on Airport Passenger Screening, and Millimeter Wave Machines. *Airport passenger screening using millimeter wave machines: compliance with guidelines*. National Academies Press, 2018. 2

[48] Akarsh Prabhakara, Tao Jin, Arnav Das, Gantavya Bhatt, Lilly Kumari, Elahe Soltanaghaei, Jeff Bilmes, Swarun Kumar, and Anthony Rowe. High resolution point clouds from mmwave radar. *arXiv preprint arXiv:2206.09273*, 2022. 2

[49] EFJ Ring and Kurt Ammer. Infrared thermal imaging in medicine. *Physiological measurement*, 33(3):R33, 2012. 3

[50] Peyman Rostami, Hojatollah Zamani, Mohammad Fakharzadeh, Arash Amini, and Farokh Marvasti. A deep learning approach for reconstruction in millimeter-wave imaging systems. *IEEE Transactions on Antennas and Propagation*, 71(1):1180–1184, 2022. 2

[51] Stefan Stojanov, Anh Thai, and James M. Rehg. Using shape to categorize: Low-shot learning with an explicit shape bias. 2021. 5, 6

[52] Yue Sun, Zhuoming Huang, Honggang Zhang, Zhi Cao, and Deqiang Xu. 3drimr: 3d reconstruction and imaging via mmwave radar based on deep learning. In *2021 IEEE In-*

ternational Performance, Computing, and Communications Conference (IPCCC), pages 1–8. IEEE, 2021. 2

[53] Yue Sun, Zhuoming Huang, Honggang Zhang, and Xiaohui Liang. 3d reconstruction of multiple objects by mmwave radar on uav. In *2022 IEEE 19th International Conference on Mobile Ad Hoc and Smart Systems (MASS)*, pages 491–495. IEEE, 2022.

[54] Yue Sun, Honggang Zhang, Zhuoming Huang, and Benyuan Liu. R2p: A deep learning model from mmwave radar to point cloud. In *International Conference on Artificial Neural Networks*, pages 329–341. Springer, 2022. 2

[55] Maxim Tatarchenko*, Stephan R. Richter*, René Ranftl, Zhuwen Li, Vladlen Koltun, and Thomas Brox. What do single-view 3d reconstruction networks learn? 2019. 6

[56] Lyne P. Tchapmi, Vineet Kosaraju, Hamid Rezatofighi, Ian Reid, and Silvio Savarese. Topnet: Structural point cloud decoder. In *2019 IEEE/CVF Conference on Computer Vision and Pattern Recognition (CVPR)*, pages 383–392, 2019. 2

[57] Texas Instruments. The fundamentals of millimeter wave radar sensors. <https://www.ti.com/lit/wp/spyy005a/spyy005a.pdf?ts=1762694207085>, 2020. 3

[58] Andreas Velten, Di Wu, Adrian Jarabo, Belen Masia, Christopher Barsi, Chinmaya Joshi, Everett Lawson, Moungi Bawendi, Diego Gutierrez, and Ramesh Raskar. Femto-photography: capturing and visualizing the propagation of light. *ACM Transactions on Graphics (ToG)*, 32(4):1–8, 2013. 3

[59] BF Wall, GM Kendall, AA Edwards, Simon Bouffler, CR Muirhead, and JR Meara. What are the risks from medical x-rays and other low dose radiation? *The British journal of radiology*, 79(940):285–294, 2006. 3

[60] Chao Wang, Feng Lin, Zhongjie Ba, Fan Zhang, Wenya Xu, and Kui Ren. Wavesdropper: Through-wall word detection of human speech via commercial mmwave devices. *Proceedings of the ACM on Interactive, Mobile, Wearable and Ubiquitous Technologies*, 6(2):1–26, 2022. 3

[61] Wenbo Wang, Wei Wang, Xixin Yu, and Weibin Zhang. C4rfnet: Camera and 4d-radar fusion network for point cloud enhancement. *IEEE Sensors Journal*, 2025. 2

[62] Guangshun Wei, Yuan Feng, Long Ma, Chen Wang, Yuanfeng Zhou, and Changjian Li. Pcdreamer: Point cloud completion through multi-view diffusion priors. In *Proceedings of the Computer Vision and Pattern Recognition Conference*, pages 27243–27253, 2025. 2

[63] Martin Weinmann, Boris Jutzi, Stefan Hinz, and Clément Mallet. Semantic point cloud interpretation based on optimal neighborhoods, relevant features and efficient classifiers. *IS-PRS Journal of Photogrammetry and Remote Sensing*, 105: 286–304, 2015. 5

[64] Tong Wu, Jiarui Zhang, Xiao Fu, Yuxin Wang, Liang Pan Jiawei Ren, Wayne Wu, Lei Yang, Jiaqi Wang, Chen Qian, Dahua Lin, and Ziwei Liu. Omniobject3d: Large-vocabulary 3d object dataset for realistic perception, reconstruction and generation. In *IEEE/CVF Conference on Computer Vision and Pattern Recognition (CVPR)*, 2023. 5, 6

[65] Peng Xiang, Xin Wen, Yu-Shen Liu, Yan-Pei Cao, Pengfei Wan, Wen Zheng, and Zhizhong Han. Snowflake point deconvolution for point cloud completion and generation with skip-transformer. *IEEE Transactions on Pattern Analysis and Machine Intelligence*, 45(5):6320–6338, 2023. 1, 2, 6

[66] Qian Xie, Qianyi Deng, Ta Ying Cheng, Peijun Zhao, Amir Patel, Niki Trigoni, and Andrew Markham. mmpoint: Dense human point cloud generation from mmwave. In *BMVC*, pages 194–196, 2023. 2

[67] Hongfei Xue, Yan Ju, Chenglin Miao, Yijiang Wang, Shiyang Wang, Aidong Zhang, and Lu Su. mmmesh: Towards 3d real-time dynamic human mesh construction using millimeter-wave. In *Proceedings of the 19th Annual International Conference on Mobile Systems, Applications, and Services*, pages 269–282, 2021.

[68] Hongfei Xue, Qiming Cao, Yan Ju, Haochen Hu, Haoyu Wang, Aidong Zhang, and Lu Su. M4esh: mmwave-based 3d human mesh construction for multiple subjects. In *Proceedings of the 20th ACM Conference on Embedded Networked Sensor Systems*, pages 391–406, 2022. 2, 3

[69] Xinguang Yan, Liqiang Lin, Niloy J. Mitra, Dani Lischinski, Danny Cohen-Or, and Hui Huang. Shapeformer: Transformer-based shape completion via sparse representation. In *Proceedings of the IEEE/CVF Conference on Computer Vision and Pattern Recognition*, 2022. 2

[70] Jiarui Yang, Songpengcheng Xia, Yifan Song, Qi Wu, and Ling Pei. mmbat: A multi-task framework for mmwave-based human body reconstruction and translation prediction. In *ICASSP 2024-2024 IEEE International Conference on Acoustics, Speech and Signal Processing (ICASSP)*, pages 8446–8450. IEEE, 2024. 2

[71] Jiarui Yang, Songpengcheng Xia, Zengyuan Lai, Lan Sun, Qi Wu, Wenxian Yu, and Ling Pei. mmdear: mmwave point cloud density enhancement for accurate human body reconstruction. *arXiv preprint arXiv:2503.02375*, 2025. 2

[72] Xumin Yu, Yongming Rao, Ziyi Wang, Zuyan Liu, Jiwen Lu, and Jie Zhou. Pointr: Diverse point cloud completion with geometry-aware transformers. In *ICCV*, 2021. 1, 2, 5, 6, 8

[73] Wentao Yuan, Tejas Khot, David Held, Christoph Mertz, and Martial Hebert. PCN: Point completion network. In *2018 International Conference on 3D Vision (3DV)*, pages 728–737. IEEE, 2018. 2

[74] Ruibin Zhang, Donglai Xue, Yuhang Wang, Ruixu Geng, and Fei Gao. Towards dense and accurate radar perception via efficient cross-modal diffusion model. *IEEE Robotics and Automation Letters*, 2024. 2

[75] Mingmin Zhao, Yingcheng Liu, Aniruddh Raghu, Tianhong Li, Hang Zhao, Antonio Torralba, and Dina Katabi. Through-wall human mesh recovery using radio signals. In *Proceedings of the IEEE/CVF International Conference on Computer Vision*, pages 10113–10122, 2019. 2

[76] Haoran Zhou, Yun Cao, Wenqing Chu, Junwei Zhu, Tong Lu, Ying Tai, and Chengjie Wang. Seedformer: Patch seeds based point cloud completion with upsample transformer. *arXiv preprint arXiv:2207.10315*, 2022. 1, 2, 8

[77] Linqi Zhou, Yilun Du, and Jiajun Wu. 3d shape generation and completion through point-voxel diffusion. In *Proceedings of the IEEE/CVF international conference on computer vision*, pages 5826–5835, 2021. 2